Volume 14
Number 17
7 September 2024
Pages 4729–5116

Catalysis Science & Technology

rsc.li/catalysis

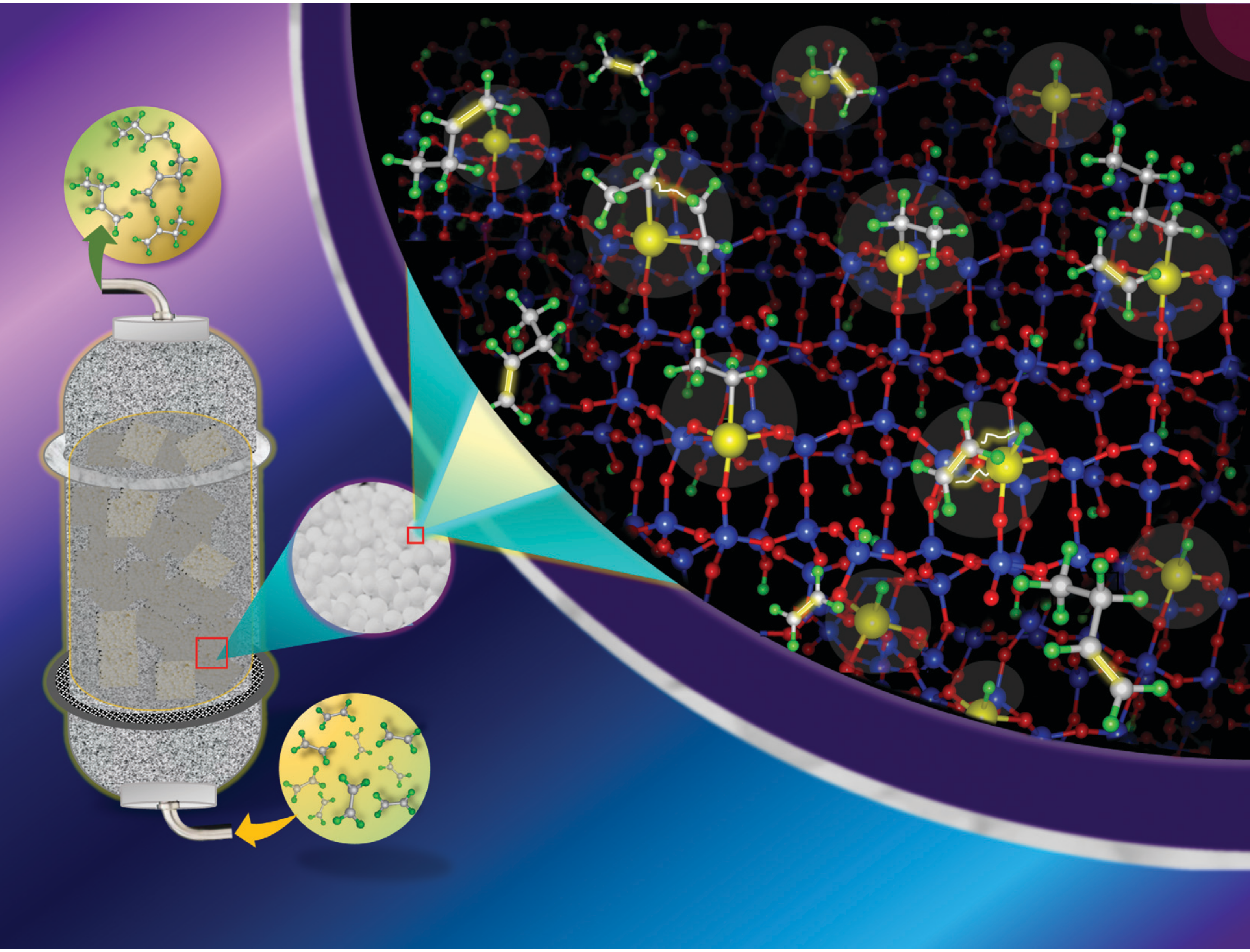

ISSN 2044-4761

ROYAL SOCIETY
OF **CHEMISTRY**

PAPER

Neha Mehra and William F. Schneider

Density functional theory and microkinetics of ethylene chain growth and termination on silica grafted group 4 metal hydrides

Catalysis
Science &
Technology

ROYAL SOCIETY
OF CHEMISTRY

PAPER

View Article Online
View Journal | View Issue

Cite this: *Catal. Sci. Technol.*, 2024, **14**, 4869

Received 30th May 2024,
Accepted 26th June 2024

DOI: 10.1039/d4cy00684d

rsc.li/catalysis

Density functional theory and microkinetics of ethylene chain growth and termination on silica grafted group 4 metal hydrides†

Neha Mehra [a] and William F. Schneider *[ab]

The creation and ethylene oligomerization function of silica-anchored group 4 metal (M = Ti, Zr, Hf) hydrides as a function of the anchor site structure are explored using density functional theory models. Oligomerization potential energy surfaces are sensitive both to the metal ion and to the structure of the anchoring site. Microkinetic models predict the oligomerization rate and degree of polymerization as a function of the site, temperature, and reactant pressures. Intrinsic catalytic activity is predicted to vary as Ti < Zr > Hf down the group, irrespective of site model, while absolute rates and product distributions are strongly sensitive to the site model, temperature, and hydrogen pressure. Catalysts based on these sites are plausible candidates for high-temperature ethylene oligomerization of interest for generating fuels from ethylene, but selectivity is expected to require careful control over the site structure and reaction conditions.

1 Introduction

Group 4 metal (M = Ti, Zr, Hf) ions anchored to oxide supports are known to catalyze a wide variety of hydrocarbon transformations.[1–4] Initially explored as heterogeneous catalysts for olefin polymerization,[5,6] anchored heterogenized ions have also been shown to activate paraffinic C–H bonds and to depolymerize paraffins.[7–12] Zakharov *et al.* demonstrated early on that group 4 tetraalkyl precursors dosed to silica and treated with hydrogen form catalysts active for ethylene polymerization at near ambient temperatures,[5,6,11] as evidenced by the appearance of vibrational features characteristic of methylene and methyl groups.[1,5,6] Depolymerization and hydrogenolysis is observed when the polymer/catalyst combination is treated in hydrogen at elevated temperatures.[1,13] Similarly prepared Ti,[7,14] Zr,[8,9,11,12] and Hf[1,10] catalysts are also observed to be active for hydrogenolysis of waxes and alkanes at 150–180 °C. These observations reflect the ability of anchored group 4 ions to form, rearrange and cleave C–C bonds, and thus their potential utility as oligomerization catalysts at elevated temperatures.

Controlled coupling of ethylene into short-chain linear alpha olefins (LAOs) or transportation fuels is particularly timely and relevant.[15] The development of shale gas reserves has created a rich new source of light hydrocarbons, including ethane.[16] Ridha *et al.* have shown that the catalytic dehydrogenation of ethane to ethylene followed by oligomerization is a potentially efficient route to liquid fuel.[17] A hydrogen-tolerant, high temperature, and selective oligomerization catalyst would obviate the need for hydrogen separation before oligomerization. In this light, hydrogen treated and supported group-4 metal catalysts are appealing candidates as potential oligomerization catalysts. As evidence of the potential, Szeto *et al.* have reported that anchored Zr is highly selective for 2-butene dimerization at an elevated pressure and temperature.[18]

The generation of anchored single-site catalysts typically takes advantage of the reaction of metal alkyl precursors with surface hydroxyls.[2,19] The precise nature of the resultant site is observed to be a function of the hydroxyl coverage.[20–22] Active catalysts are prepared by treatment in hydrogen to remove residual alkyls and form surface hydrides.[7,14,21,23–25] These processes have been investigated spectroscopically using vibrational infrared (IR), $^{1}H/^{29}Si$ and $^{1}H/^{13}C$ solid state nuclear magnetic resonance (NMR) and ^{1}H double-quantum (DQ) solid-state NMR, and extended X-ray absorption fine structure (EXAFS) spectroscopies, as well as chemical methods. When tetraalkyl group 4 precursors are dosed to silica, typical products after hydrogen treatment include mono-($(\equiv SiO)_3MH$) and dihydrides ($(\equiv SiO)_2MH_2$).[1,8,12,24–26]

Guided by these observations, atomistic representations of silica-anchored group 4 ions have been attempted by cluster and periodic approaches that use silica models of different

---

[a] Department of Chemical and Biomolecular Engineering, University of Notre Dame, Notre Dame, IN 46556, USA. E-mail: wschneider@nd.edu

[b] Department of Chemistry and Biochemistry, University of Notre Dame, Notre Dame, IN 46556, USA

† Electronic supplementary information (ESI) available. See DOI: **https://doi.org/10.1039/d4cy00684d**

types and sizes.[24,27–31] Cluster models capture local site structure and approximate the constraints imposed by the larger silica framework. Mono- and dihydrides of Zr or Ti have been grafted on clusters composed of two to three silicon atoms for evaluating energy profiles of methane activation, ethylene chain growth and hydrogenolysis of M-alkyl reactions.[3,28,31–33] Kalhor *et al.* investigated the reactivity of similarly modeled Zr-hydrides towards N_2O and CO_2 probe molecules and found predicted IR and NMR signatures to be consistent with experimental observations.[34] β-Cristobalite is a popular choice[35,36] for describing a silica support, because it can be simply represented within a supercell, it incorporates the constraints of the bulk oxide, and its (111)- and (001)-facets have local order similar to amorphous silica, based on X-ray diffraction observations.[37] Approximate models of amorphous silica have been constructed through molecular dynamics simulations starting from a fully hydroxylated β-cristobalite surface[38,39] or other siliceous structures.[36,40,41] The reactivity is reported to be sensitive to the details of the support model, whether represented as a cluster,[42,43] a pseudo-amorphous structure,[30,44–46] or an ordered β-cristobalite surface.[27,36] The "right" balance of strain,[44,45] topological orientation,[43] and relative site abundance[47–49] are all reported to have an impact on reactivity. In general, there is no agreement on the appropriate strategy or exact relationship between the representation of the anchoring site and reactivity.[50]

From the available experimental[5,51,52] and computational[3,33,53,54] evidence, supported metal hydrides catalyze olefin chain growth through olefin insertion into M–H bonds (reaction (1)) and into M–C bonds (reaction (2)):

$$\mathrm{M{-}H + C_2H_4(g) \rightarrow M{-}C_2H_5} \tag{1}$$

$$\mathrm{M{-}C_2H_5 + C_2H_4(g) \rightarrow M{-}C_4H_9} \tag{2}$$

Termination may occur through hydride elimination to the metal (reaction (3a)), chain transfer to a monomer (reaction (3c)),[55] or alkyl elimination (reaction (3b)):[7–9]

$$\mathrm{M{-}C_4H_9 \rightarrow M{-}H + C_4H_8(g)} \tag{3a}$$

$$\mathrm{M{-}C_4H_9 \rightarrow M{-}C_2H_5 + C_2H_4(g)} \tag{3b}$$

$$\mathrm{M{-}C_4H_9 + C_2H_4(g) \rightarrow M{-}C_2H_5 + C_4H_8(g)} \tag{3c}$$

$$\mathrm{M{-}C_4H_9 + C_2H_4(g) \rightarrow M{-}C_2H_3 + C_4H_{10}(g)} \tag{3d}$$

Lastly, ethylene-mediated alkane elimination (reaction (3d)) has been proposed as a competing termination step, based on early computational work.[54,56]

Besedin *et al.* compared pathways relevant to ethylene polymerization (reactions (1) and (2)) on cluster models of Zr mono- and dihydrides.[33] They reported activation energies for insertion of ethylene into M–C bonds (reaction (2)) to be greater than insertion into the M-hydride (reaction (1)), making the former rate limiting for chain growth. Similar models of Ti mono- and dihydrides predict M–C insertion barriers to be greater than that for Zr,[3] suggesting a role of the metal ion in controlling chain growth. Their work did not comment upon the role of termination pathways (reactions (3a)–(3d)).

Kaminsky *et al.*,[57] Hoffman *et al.*,[58] and Kissin *et al.*[59] reported that co-fed H_2 reduces the polymer average molecular weight relative to a pure ethylene feed, suggesting that hydrogenolysis of the M–R bond competes with chain growth:[1,13]

$$\mathrm{M{-}R + H_2(g) \rightarrow MH + RH} \tag{4}$$

Reaction (4) is a σ-bond metathesis and results in hydrogenolysis of the M-alkyl group. Prior first principles studies have focused on M-butyl hydrogenolysis to form butane in the context of chain termination.[3,33] The relative contributions of reaction (4) and reactions (2), (3a), (3b), (3c) and (3d) will depend on relative activation energies and reaction conditions, highlighting the need for microkinetic modeling to identify combinations of metal ions and conditions that yield desirable product ranges. Other side reactions, like reinsertion of olefin products that lead to chain walking, isomerization, and methane (see Scheme S1†), can influence product topology, type and final properties but are less relevant to intrinsic average molecular weight, which depends upon the competition between chain growth and termination.[2]

To address this need, here we use supercell DFT models to compare ethylene chain growth and termination pathways (reactions (1) to (4)) on group 4 metal hydrides grafted on silica. We construct models to probe the sensitivity of energetics to metal ion identity and nature of the anchoring site. We find non-periodicity in kinetics with Zr sites having the lowest activation energies for all reaction steps, followed by Hf and Ti sites, irrespective of the hydrides considered. However, we observe that chain growth kinetics are sensitive to the host silica ring size. We use the DFT results as inputs to microkinetic models to predict turnover frequencies and degree of polymerization ($\bar{P}_n$) as a function of the metal ion, site environment and hydrogen pressures at various temperatures. We show that the rate and $\bar{P}_n$ are sensitive to both the metal ion and anchoring site. We conclude that these isolated ions are candidates to synthesize fuel range to polymeric products from ethylene, given that the control is exercised over synthesis protocols, reaction conditions and feed composition.

2 Methods

2.1 Computational details

Plane-wave, supercell DFT calculations are performed using the Vienna *Ab initio* simulation package (VASP),[60–63] and projector augmented wave[64] treatment of core-valence interactions. All systems studied are closed shell and were treated non-spin-polarized using the Perdew–Burke–Ernzerhof (PBE) generalized gradient approximation (GGA).[65,66] The Brillouin zone is sampled at the Γ point, plane waves are included to a cutoff of 400 eV, and self-consistent field electronic energies converged to 10^{-6} eV. Atomic forces are converged to less than 0.05 eV Å^{-1} using a conjugate gradient algorithm. Transition states are constructed using a climbing image nudged elastic band (CI-NEB)[67,68] by linearly interpolating between initial and final structures. Final clean up of transition states was performed using a quasi-Newton (variable metric) optimization or the dimer method.[69] Transition states are confirmed through harmonic frequencies and by visual inspection of imaginary modes in the graphical interface of the atomic simulation environment (ASE).[70] Harmonic vibrational frequencies of the species are computed by finite difference with a step size of 0.01 Å including all adsorbate atoms, metal atom, and/or oxygens of the first coordination sphere. Free gas molecules are put in 15 × 15 × 15 Å^3 cubic cells; energies are given in Table S1.† Electronic energies of reaction intermediates and transition states are reported in Tables S7, S13, S19† and reaction and activation energies for elementary steps in Tables S8, S14 and S20.† All energies reported in electron volts (eV) where 1 eV = 23.06 kcal mol^{-1} = 96.5 kJ mol^{-1}. Molecular visualizations are created using VESTA.[71]

We built baseline silica surface models starting from cubic ($Fd3m$) β-cristobalite (Fig. S1a†).[72] Within the optimization parameters used here, the relaxed bulk lattice constant is 7.23 Å (experimental: 7.16 Å). The 1% overestimation is typical for gradient-corrected functionals.[27,73] Silica surfaces having Si–OH groups are created by cleaving Si–O bonds of β-cristobalite along the (111) and (001) planes[74] and saturating oxygen and silicon dangling bonds with H and OH, respectively. Fully relaxed slabs are shown in Fig. S1b and S1c.† The surface hydroxyl density of the (111) and (001) models are 3.8 and 7.6 OH per nm^2, respectively. Metal complexes are anchored on these surface hydroxyls or silanols (Si–OH). We also reconstruct these surfaces to modify the support environment around the metal sites. Overall, we compare three distinct metal hydride site models (Fig. S2†). The first two models are of $(\equiv\text{SiO})_3\text{MH}$ situated on three Si–OH groups of isolated silanols (separated by –O–Si–O– bonds) and of vicinal silanols (separated by –O– bonds) on the (111) silica surface, while the third is of $(\equiv\text{SiO})_2\text{MH}_2$ anchored on a pair of vicinal Si–OHs of (001) silica. We refer to sites as ***a*-*b*mr** $(\equiv\text{SiO})_{4-n}\text{MH}_n$ where ***a*** is the number of rings and ***b*** is the membered ring (mr) size formed by consecutive M–OSi bonds with the silica support. Further model details are provided below.

2.2 Microkinetic models

We use the DFT results to parameterize mean-field microkinetic models. The net rate of surface reaction j over time t is written as:

$$r_j = k_{+j}\prod_{+j}\theta_{+j}^{-c_{ij}}\prod_{+j}P_{+j}^{-c_{ij}} - k_{-j}\prod_{-j}\theta_{-j}^{c_{ij}}\prod_{-j}P_{-j}^{c_{ij}} \tag{5}$$

where c_{ij} is the stoichiometric coefficient for species i in reaction j. The forward and backward reactions are represented as $+j$ and $-j$, respectively. k_j is the rate constant and θ_j and P_j are the coverages and pressures of different species involved in reaction j, respectively. The coverage is conserved for a surface:

$$\theta_* + \sum_i \theta_i = 1 \tag{6}$$

where θ_* is the coverage of free sites. At steady state, $\sum_j c_{ij}r_j = 0$, giving linear algebraic equations that are solved symbolically with the SymPy[75] library and then numerically in Python[76] to obtain steady-state coverages at each temperature and pressure condition. Steady state rates (s^{-1}) or turnover frequencies (TOFs) are obtained from these coverages.

Rate constants for non-activated adsorption of species i are calculated using the Hertz–Knudsen equation (eqn (7)), where α' is a sticking coefficient that we take as unity, m_i is the molecular weight of the adsorbing species, k_B is the Boltzmann constant, T is the temperature, and A is the area per free site, which we approximate as the surface area of the unit cell. This approximation likely exaggerates A, thus increasing absolute adsorption rates, but is unlikely to influence reactivity trends.

$$k_{\text{ads},i} = \frac{\alpha' A}{\sqrt{2\pi m_i k_B T}} \tag{7}$$

Desorption rate constants are written assuming reaction equilibrium:

$$k_{\text{des},j} = \frac{k_{\text{ads},i}P^\circ}{K_j(T)} \tag{8}$$

where $K_j(T)$ is the equilibrium constant of reaction j, given by

$$K_j(T) = \exp\left(-\frac{\Delta E^{\text{DFT}}_{\text{ads},j} + \Delta E^{\text{ZPE}}_{\text{ads},j} - T\Delta S^\circ_{\text{ads},i}(T)}{k_B T}\right) \tag{9}$$

ΔE^{ZPE} is the zero-point energy (ZPE) correction added to the electronic energy change ΔE^{DFT}. Similar to Toch *et al.*,[77] we take the entropy of physisorption, $\Delta S^\circ_{\text{phys},i}(T)$ to be $-1/3S^\circ_{\text{trans},i}(T)$, where $S^\circ_{\text{trans},i}(T)$ is the translational entropy of the gas-phase species i calculated by the Sackur–Tetrode equation.[78,79]

Surface reaction rate constants (k) are calculated using transition state theory, DFT-computed and ZPE corrected activation energies $E_{\text{a},j}$ and the entropy change $\Delta S_j^\ddagger(T)$.

$$k = \frac{k_B T}{h}\exp\left(\frac{\Delta S_j^\ddagger}{k_B}\right)\exp\left(-\frac{E_{\text{a},j}}{k_B T}\right) \tag{10}$$

$\Delta S_j^\ddagger(T)$ between a physisorbed species and a transition state is $-\frac{2}{3}S^\circ_{\text{trans},i}(T)$ and that between a chemisorbed species and a transition state is zero. Test calculations show that the relative entropy changes are similar to those obtained from the harmonic oscillator and rigid rotor approximation for adsorbates. The free energy change of an elementary reaction (ΔG_j°) is approximated as

$$\Delta G_j^\circ(T) = \Delta E_j^{\mathrm{DFT}} + \Delta E_j^{\mathrm{ZPE}} - T\Delta S_j^\circ(T) \tag{11}$$

Reaction free energies are plotted in Fig. S8, S9, S13, S18 and S19.†

3 Results and discussion

3.1 3-4mr $(\equiv\mathrm{SiO})_3\mathrm{MH}$ site construction

We compute the energies to graft model tetraalkyl $M(CH_3)_4$ precursors to the silica (111) surface shown in Fig. S1b,† whose adjacent Si–OH groups are separated by –O–Si–O– linkages. The choice of the precursor mimics the organometallic precursors typical for grafting metals. Grafting creates covalent M–O–Si linkages, resulting in $(\equiv\mathrm{SiO})_n\text{–}\mathrm{M}(\mathrm{CH}_3)_{4-n}$ species that vary in their degree of coordination to the support, n (details on page 5 in the ESI†). Fig. S3† shows the relaxed structures for n = 1, 2, 3 and Table S2† has their energies. The energies of successive grafting steps of the $Zr(CH_3)_4$ precursor on the (111) surface (Fig. S4a†) indicate that the Zr species tri-coordinated to the support (n = 3) is the most thermodynamically favored. A parity plot of integral grafting energies for all metal ions (values in Table S3†) against Zr as shown in Fig. S4b† highlights the exothermic trend to be Ti < Zr < Hf, in line with the reported M–O and M–C bond energies (Table S4†).[80] Successive grafting energies decrease in magnitude with increasing degree of grafting, likely reflecting accumulated strain.

We next compute the energy to remove residual $-CH_3$ ligands with hydrogen. Hydrogenolysis of each $(\equiv\mathrm{SiO})_n\text{-}\mathrm{M}(\mathrm{CH}_3)_{4-n}$ to form the corresponding hydride (Table S2†) is exothermic (Table S3†). Relaxed $(\equiv\mathrm{SiO})_n\mathrm{M}(\mathrm{H})_{4-n}$, M = Ti, Zr, Hf, structures are shown in Fig. S5.† M–O and M–H bond lengths in the tetrahedral M-hydride sites vary non-periodically as Ti < Hf ≤ Zr, following their ionic radii.[81,82] The average O–M–H angle in $(\equiv\mathrm{SiO})_3\mathrm{M}(\mathrm{H})$ also follows the same trend. Overall, Ti sites have the least negative formation energies, referenced to silica (111) and the precursor.

Fig. 1 shows a representative modeled metal monohydride, $(\equiv\mathrm{SiO})_3\mathrm{MH}$ on silica (111), obtained upon full relaxation. The metal ion forms three M–O–Si bonds to the support and thus, rests upon three 4-membered rings (**3-4mr**), each containing three Si and a metal ion (Si/Si/Si/M). Oxygen atoms are excluded while naming the ring. Adjacent M–O–Si bonds are separated by O–Si–O linkages. We name this model as **3-4mr** $(\equiv\mathrm{SiO})_3\mathrm{MH}$, where 3 is for the number of rings it forms with silica and 4 refers to the size of each ring. Computed M–H stretch vibrations of **3-4mr** $(\equiv\mathrm{SiO})_3\mathrm{MH}$ in the harmonic limit agree well with experimentally reported frequencies (Table S5†). These results are consistent with the well-known ability of a hydroxyl covered silica surface to accommodate metal alkyl precursors and their further conversion to thermodynamically stable hydrides.

3.2 Oligomerization intermediates on 3-4mr $(\equiv\mathrm{SiO})_3\mathrm{MH}$ sites

To evaluate the sensitivity of ethylene oligomerization to the metal ion, we computed reaction pathways for ethylene insertion and chain growth, steps 1 through 4 in Fig. 2, including the three competing chain termination routes, on the **3-4mr** $(\equiv\mathrm{SiO})_3\mathrm{MH}$ models. Transition states (TSs) are labeled according to the corresponding reaction number. Multiple configurations of each intermediate were explored, and the lowest-energy structures and corresponding transition states are shown in Fig. S6.† CONTCARs are available in a Zenodo data repository. Based on geometry data in Table S6,† the Ti species have the widest O–M–O angle and the shortest M–H or M–C bonds. The Hf species have slightly shorter bond lengths than the Zr species. CI-

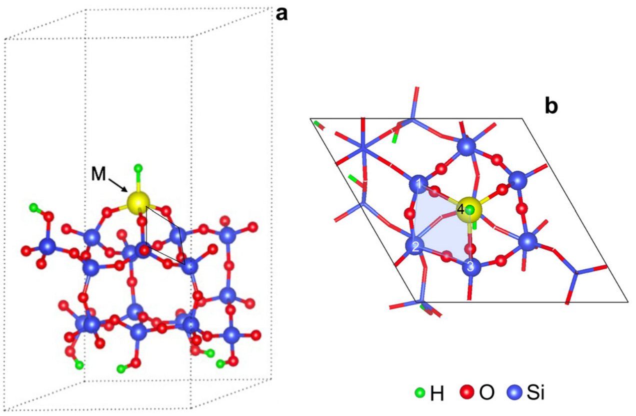

Fig. 1 Representative supercell of **3-4mr** $(\equiv\mathrm{SiO})_3\mathrm{MH}$ on silica (111): (a) side view with edges of a **4mr** (Si/Si/Si/M) ring marked; (b) top view shows M sitting on three **4mr**(s) with one ring shaded and numbered. Only Si and O atoms of the rings connected to the metal are highlighted.

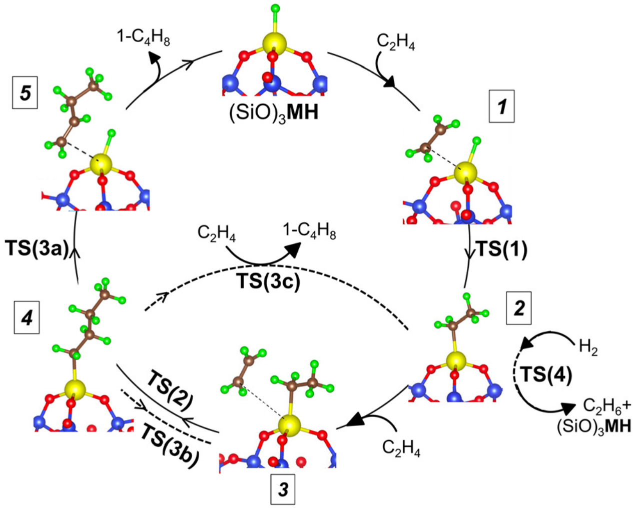

Fig. 2 Ethylene oligomerization cycle on $(\equiv\mathrm{SiO})_3\mathrm{MH}$.

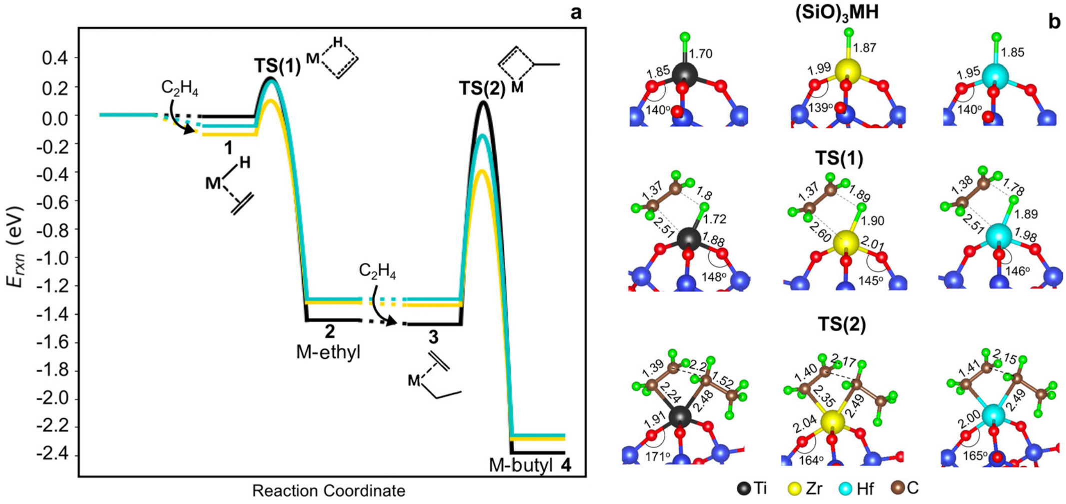

Fig. 3 (a) Cossee–Arlman potential energy surfaces computed and referenced to **3-4mr** (≡SiO)$_3$MH sites and $2C_2H_4$ gas molecules for M = Ti (black), Zr (yellow) and Hf (blue). Species numbers correspond to Fig. 2. (b) Structures of **3-4mr** (≡SiO)$_3$MH, TS(1) and TS(2). Bond distances in Å and bond angles in °.

NEB trajectories are shown in Fig. S7.† Electronic energies of the structures are given in Table S7† and the DFT-computed reaction and activation energies for elementary steps are in Table S8.†

Potential energy surfaces (PESs) for ethylene insertion and chain growth are reported in Fig. 3a. The calculations reveal ethylene physisorbs on the hydride site (structure **1** in Fig. 2 and 3a) with some distortion of the O_3MH tetrahedron. The binding energies are modestly negative. Ethylene inserts into the M–H bond through a four-membered-ring transition state, TS(1) (Fig. 3b), to generate M-ethyl (structure **2**). TS(1) structures are relatively insensitive to metal ions, except for the noticeable difference in the Si–O–M angle that is widest for Ti. Activation energies relative to the hydride and ethylene range from −0.02 to 0.12 eV. Reaction energies from the hydride to the ethyl are slightly greater on Ti (by −0.14 eV) than those on Zr and Hf (1*, 1 in Table S8†). The results suggest that ethylene insertion into the hydride will be rapid and roughly insensitive to the metal.

Ethylene adsorption at M-ethyl occurs with little distortion of the O_3MC tetrahedron (structure **3** in Fig. 2) and ethylene sits away from and weakly bound to the metal center (Fig. S6† and 3a, 2* in Table S8†). A representative CI-NEB trajectory for migratory insertion of ethylene into the M–C bond of M-ethyl *via* the TS(2) on the Hf site forming the C–C bond is shown in Fig. S7b.† The initially bent butyl chain then rotates to an elongated, zig-zagged M-butyl that is lower in energy (structure **4** in Fig. 2). Migratory insertion into the M–C bond has a substantially greater barrier that decreases from Ti > Hf > Zr, in inverse variation to the M–C and M–O bond lengths. Ustynyuk *et al.*[3] similarly report higher M–C insertion activation energies for Ti-monohydride than that for Zr on cluster models. Ethylene is closest to Ti in the TS(2) (shown in Fig. 3b) due to its smallest ionic radius. The Si–O–Ti angle increases to 171°, 6° more than the Si–O–Hf and Si–

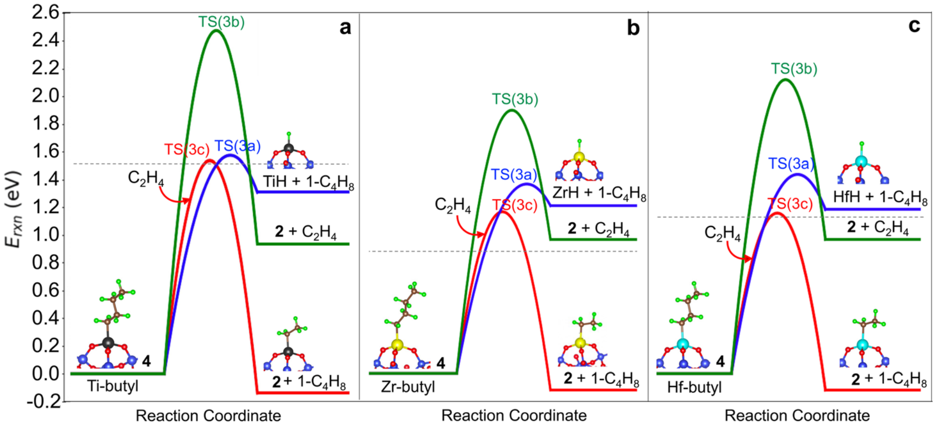

Fig. 4 Comparison of termination by β-H elimination (blue), β-alkyl transfer (green), and β-H transfer to ethylene (red) on **3-4mr** grafted (a) (≡SiO)$_3$TiC$_4$H$_9$, (b) (≡SiO)$_3$ZrC$_4$H$_9$, and (c) (≡SiO)$_3$HfC$_4$H$_9$ sites. Dashed lines indicate energy barriers for chain growth via ethylene insertion.

O–Zr angles. The average strain induced by stretching of the Si–O–M angles as the site passes through a TS is measured by $\langle a \rangle$ and is reported in Table S9.† For the TS(2), $\langle a \rangle$ varies with the barrier of migratory insertion into the M–C bond and decreases from Ti to Hf to Zr. Thus, a larger $\langle a \rangle$ indicates a greater structural distortion associated with a larger energy penalty for reaching the TS.

We compare the three termination pathways (reactions (3a)–(3c)) in Fig. 4a, b and c, respectively. Overall, the three termination routes have barriers comparable to or greater than chain growth (dashed line in Fig. 4a–c). Termination by reaction (3a) occurs *via* the TS(3a) (structure in Fig. S6†) and involves β-H transfer from M-butyl to the metal ion. Simultaneous loss of the M–C bond yields 1-butene adsorbed on $(\equiv SiO)_3MH$ (structure **5** in Fig. 2). Ti has the highest activation energy for this step, followed by Hf and then Zr. Butene binds weakly to the metal ion (3a* in Table S8†). This pathway is the reverse of ethylene insertion into the M–H bond and there is an orientational resemblance between the TS(3a) and TS(1).

Transfer of a β-alkyl fragment to M releases an ethylene molecule from the growing chain (reaction (3b)) and thus is the reverse of reaction (2). We replot the computed energy profile of the latter, referenced to M-butyl, **4**, in Fig. 4a–c. Activation energies increase from Zr to Hf to Ti and are greater than β-H to M activation energies by at least 0.55 eV.

The TS(3c) for ethylene-assisted termination (reaction (3c)) is obtained by coordinating an ethylene to M-butyl and simulating a direct transfer of H from the β-C of the butyl chain to ethylene (CI-NEB in Fig. S7d†), yielding 1-butene and M-ethyl. TS(3c) is a 6-membered ring and is geometrically similar on Ti, Zr, and Hf (structures in Fig. S6†). Fig. 4a–c shows that reaction (3c) is slightly exothermic, unlike reactions (3a) and (3b). This route is kinetically favored over β-H transfer to M on Ti-, Zr- and Hf-butyl. However, the entropic cost to coordinate an ethylene to M-butyl also enters into the contribution of this route, as discussed further below.

Hydrogenolysis of the M–C bond via reaction (4) would also terminate the growing chain. We computed H_2 dissociation across the M–C bond of M-ethyl (2) to form ethane and restore $(\equiv SiO)_3MH$ (reaction (4)) *via* the TS(4) (Fig. S7e†). Fig. 5 shows that C–C bond formation yielding M-butyl (**4**) is more exothermic than hydrogenolysis to ethane (reactions 2*, 2, 4*, 4 in Table S8†). Barriers are comparable on Zr-ethyl and lower for hydrogenolysis on Ti- and Hf-ethyl. The resultant ethylene hydrogenation ($C_2H_4 + H_2 \rightarrow C_2H_6$) is highly exothermic (−1.40 eV). Hydrogen will likely impact both overall chain growth and selectivity to olefinic products.

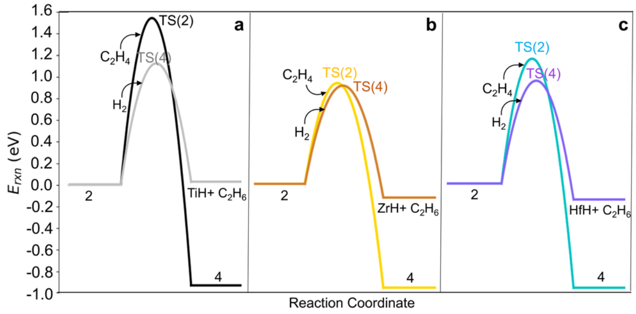

Fig. 5 Comparison of potential energy surfaces for ethylene migratory insertion into M–C bond *via* the TS(2) and hydrogenolysis *via* the TS(4) on **3-4mr** $(\equiv SiO)_3MC_2H_5$, **2** for M = (a) Ti, (b) Zr and (c) Hf, each referenced to site 2 and the gas molecule (H_2 or C_2H_4) reacting with it.

These findings show that the key steps of chain growth and termination by chain transfer to the ethylene monomer are highly sensitive to the nature of the group-4 metal ion and will impact overall reaction chemistry. Differences in initiation steps and hydrogenolysis also exist, but are modest.

3.3 Oligomerization microkinetics on 3-4mr $(\equiv SiO)_3MH$ sites

We use DFT-computed reaction and activation energies to formulate a fully reversible microkinetic model. Adsorbates are assumed to lose all translational entropy and to retain all rotational and vibrational entropy; a harmonic oscillator and rigid rotor model yields nearly equivalent results (Fig. S8†). We include initiation, chain growth and β-H transfer to the metal with the model. Other termination pathways are kinetically uncompetitive at the temperatures probed here (Fig. S9†). Calculations on homogeneous Ti-alkoxide complexes similarly report a preference for the β-H to M termination pathway.[83] As our goal is to compare ideal rates and selectivities to olefin *vs.* paraffin products *vs.* the metal, we neglect reinsertion reactions and chain-walking processes, which can lead to isomerized chains and secondary products. Thus, we focus on primary reaction channels, and assume that transport of products from active sites is more rapid than reinsertions.

Steady state rates are computed at zero conversion in pure ethylene feed at 17 bar pressure to capture the intrinsic activities. Computed turnover frequencies (TOFs) are shown as an Arrhenius plot in Fig. 6. TOFs vary as Zr > Hf > Ti,

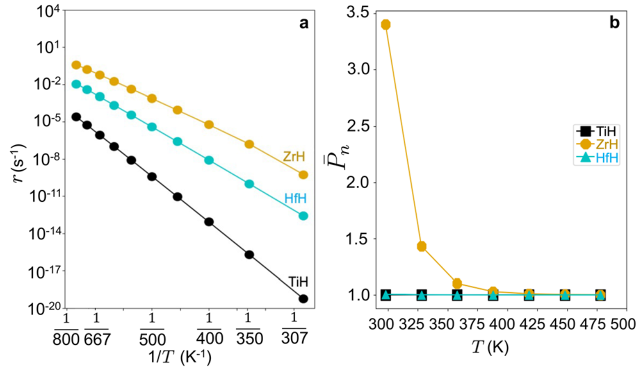

Fig. 6 (a) Oligomerization rates (r) at $P_{C_2H_4}$ = 17 bar against reciprocal temperature (1/T) and (b) $\bar{P}_n$ *vs.* temperature (T) on **3-4mr** $(\equiv SiO)_3MH$ sites (M = Ti, Zr, Hf).

opposite apparent activation energy trends. Fig. S10† shows that Hf-ethyl and Ti-ethyl are the most abundant surface intermediate (MASI) at all temperatures, while the MASI evolves from Zr-butyl to Zr-ethyl with increasing *T*.

To identify the elementary steps most responsible for controlling the dimerization rates, degree of rate control (DRC)[84] analysis is performed. The rate sensitivity to specific reactions is calculated as $X_{\mathrm{RC},j}$ (eqn (12)) by changing the forward (k_{+j}) and reverse (k_{-j}) rate constants of step *j* simultaneously by 2%, and monitoring the change of the overall rate *r* with respect to the reference rate, r_0. The rate constants of other steps and the equilibrium constant, K_j, are kept constant.

$$X_{\mathrm{RC},j} = \frac{\partial \ln r}{\partial \ln k_j} \approx \frac{r - r_0}{0.02 \times r_0} \tag{12}$$

M–C insertion is rate controlling on the TiH and HfH sites (Fig. S11†) at all temperatures, while β-H termination limits the ZrH rate at low *T* and M–C insertion at higher *T*.

We employ DFT rate constants to first estimate the degree of polymerization ($\bar{P}_n$) promoted by each metal site on the reaction with olefins and in the absence of H_2. The $\bar{P}_n$ model assumes that chain growth occurs with a probability of propagation, α,[85,86] calculated by steady state mole balance applied to an M-alkyl site assuming all reactions are irreversible and rate constants for chain growth, k_{cc} and termination, k_{term} are independent of chain length (eqn (S11), details in the ESI,† page 21). The $\bar{P}_n$ value for ethylene only feed expresses the average number of oligomeric units[86,87] in the olefinic product:

$$\bar{P}_n = \frac{1}{1-\alpha} = 1 + \frac{k_{\mathrm{CC}}}{k_{\mathrm{term}}} P_{\mathrm{C_2H_4}} \tag{13a}$$

$$\bar{P}_n = 1 + \exp\left(\frac{\Delta S^{\ddagger}_{\mathrm{CC}} - S^{\ddagger}_{\mathrm{term}}}{k_{\mathrm{B}}}\right) \cdot \exp\left(\frac{E_{\mathrm{a,term}} - E_{\mathrm{a,CC}}}{k_{\mathrm{B}} T}\right) P_{\mathrm{C_2H_4}} \tag{13b}$$

Eqn (13b) deconvolutes the entropic and activation energy contributions to $\bar{P}_n$. The calculated $\bar{P}_n$ values are shown in Fig. 6b and follow Ti ≤ Hf < Zr. $\bar{P}_n$ is a decreasing function of temperature and is greatest on Zr. Thus, within the **3-4mr** site model, ZrH is expected to be a more effective catalyst than TiH or HfH, each of which would have little to any oligomerization activity. Such small $\bar{P}_n$ stands in contrast to experimental observations of polymerization by group-4 metal hydrides on silica.[1,5,6,11] $\bar{P}_n$ on a **3-4mr** ZrH site at low ethylene pressure is approximately one (Fig. S12b†). This observation suggests that some feature of the model other than the metal itself is relevant to the catalysis.

Hydrogenolysis will compete with β-H elimination with co-fed H_2(g). To incorporate this competition into the $\bar{P}_n$, α is recast as $\alpha_{\mathrm{H_2}}$ (eqn (14a) and (S12)†). The contributions of olefin and paraffin to total $\bar{P}_n$ (computed with $\alpha_{\mathrm{H_2}}$) are obtained by multiplying this $\bar{P}_n$ by the ratio of individual fraction's production rate to the total rate of product formation:

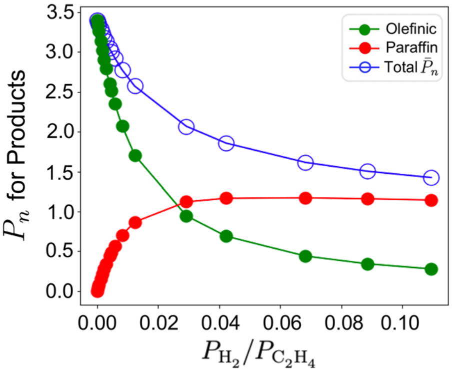

Fig. 7 Total $\bar{P}_n$ on the **3-4mr** (≡SiO)$_3$ZrH site and relative contributions of olefin (green) and paraffin (red) fractions to it against $P_{\mathrm{H_2}}/P_{\mathrm{C_2H_4}}$ at *T* = 298 K and total pressure of 17 bar.

$$\alpha_{\mathrm{H_2}} = \frac{k_{\mathrm{cc}} P_{\mathrm{C_2H_4}}}{k_{\mathrm{cc}} P_{\mathrm{C_2H_4}} + k_{\mathrm{term}} + k_{\mathrm{hyd}} P_{\mathrm{H_2}}} \tag{14a}$$

$$\text{Olefinic Product} = \bar{P}_n \cdot \frac{k_{\mathrm{term}}}{k_{\mathrm{term}} + k_{\mathrm{hyd}} P_{\mathrm{H_2}}} \tag{14b}$$

$$\text{Paraffin Product} = \bar{P}_n \cdot \frac{k_{\mathrm{hyd}} P_{\mathrm{H_2}}}{k_{\mathrm{term}} + k_{\mathrm{hyd}} P_{\mathrm{H_2}}} \tag{14c}$$

We vary $P_{\mathrm{H_2}}/P_{\mathrm{C_2H_4}}$ such that the total pressure is always 17 bar and trace the resultant modulation in $\bar{P}_n$ values at 298 K and 473 K. Rate constants are computed from entropy-corrected energy profiles (Fig. S13†). At 298 K, a decrease in $\bar{P}_n$ can be seen for the **3-4mr** (≡SiO)$_3$ZrH site along with the increasing dominance of paraffinic products even when a small amount of hydrogen is added (0–0.1 molar ratio, Fig. 7). The same behavior is seen for Ti and Hf (Fig. S13†), but the decline in $\bar{P}_n$ is not significant. $\bar{P}_n$ at 473 K on the three **3-4mr** (≡SiO)$_3$-MH sites shown in Fig. S13† is close to unity and the sites are inactive for ethylene hydrogenation.

3.4 Influence of the anchoring site

To explore the sensitivity of the results above to the silica anchoring site, we considered a model in which the M ion is anchored *via* three 3-membered-rings (**3-3mr**) to silica (Fig. 8a). We adopt the reconstructed silica (111) facet to represent the host site (Fig. S14†), yielding an environment similar to prior cluster models,[3,33] and focus on M = Zr for the comparisons. Fig. S16† shows the structures and Tables S10 and S11† report the energies to form (≡SiO)$_n$–Zr(CH$_3$)$_{4-n}$ (n = 1–3) by Zr(CH$_3$)$_4$ grafting and hydrogenation to (≡SiO)$_n$–Zr(H)$_{4-n}$ (plot in Fig. S15a†). Grafting energies are less exothermic than on the more open **3-4mr** site (parity plot in Fig. S15b†), as is hydrogenolysis. Bond distances are similar across the two models, but Zr–O–Si angles are less obtuse at the more constrained **3-3mr** site. The M–H stretch frequency is red shifted 36 cm^{-1} relative to the corresponding **3-4mr** (≡SiO)$_3$ZrH.

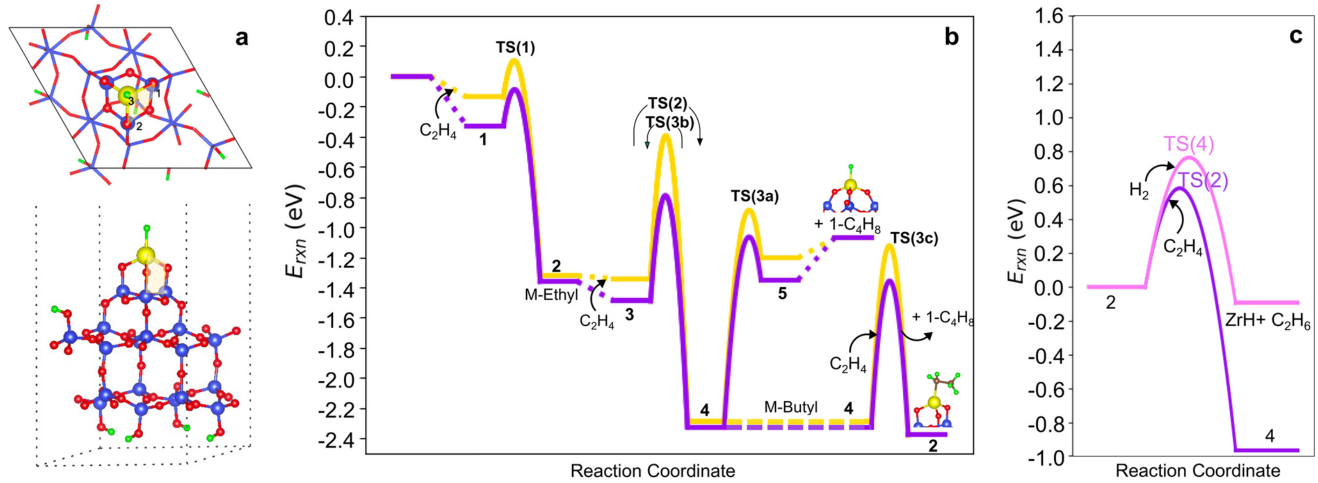

Fig. 8 (a) Top and side views of **3-3mr** $(SiO)_3ZrH$ site. (b) Comparison of **3-4mr** (yellow) and **3-3mr** (purple) ZrH ethylene dimerization PESs computed and referenced to the site and number of C_2H_4 molecules reacting with it. Species numbers correspond to Fig. 2. (c) Migratory insertion into the M–C bond (purple) and hydrogenolysis (pink) pathways on **3-3mr** $(\equiv SiO)_3ZrH$ sites.

We computed the same ethylene insertion and termination pathways on the **3-3mr** $(\equiv SiO)_3ZrH$ site. The structures are shown in Fig. S17,† bond distances and angles in Table S12,† energies in Table S13,† and reaction and activation energies in Table S14.† Fig. 8b compares the reaction profiles on the **3-3mr** and **3-4mr** sites. The energies of the intermediates are nearly the same in the two models, while olefin physisorption (points 1, 3, and 5) is somewhat more exothermic within the more strained **3-3mr** model. Activation barriers for chain growth (TS(2)) and for the three termination routes TS(3a–c) are 0.2 eV less within the **3-3mr** model as is the extent of $\langle a \rangle$ as the TSs are approached (Table S15†). The O–M–H angle increases 8° from the **3-4mr** to the **3-3mr** model, reflecting an increase in access of olefin to the metal site in the latter case. β-H transfer has the lowest activation barrier of all termination routes independent of the site model. In contrast, ethylene insertion has a lower activation energy than hydrogenolysis in the **3-3mr** model (Fig. 8c), opposite that observed for the **3-4mr** case.

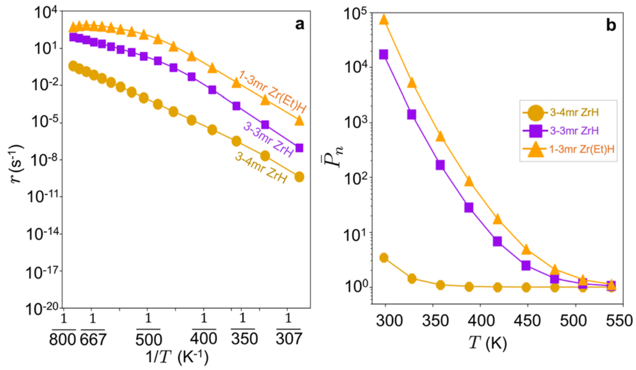

Fig. 9 (a) Oligomerization rate (r) *vs.* reciprocal temperature (1/T) and (b) log $\bar{P}_n$ *vs.* temperature (T) on **3-4mr**, **3-3mr** $(\equiv SiO)_3ZrH$ and **1-3mr** $(SiO)_2Zr(Et)H$ sites at $P_{C_2H_4}$ = 17 bar.

To compute the oligomerization rates, we again took β-H transfer to M to be the dominant termination pathway based on a free energy analysis (Fig. S18a and b†) and computed rates using the same initiation, growth, and termination model. Fig. 9a compares the computed rates on the **3-3mr** and **3-4mr** sites at elevated ethylene pressure. The rates are two- to three-orders of magnitude greater on the **3-3mr** site. DRC analysis reports the same shift from β-H termination to ethylene insertion with increasing temperature (Fig. S18d†), in correspondence with a shift of the MASI (Fig. S18c†) from Zr-butyl to Zr-ethyl. The ethylene-only $\bar{P}_n$ on the **3-3mr** site (Fig. 9b) is similarly significantly increased than that on the **3-4mr** site (Fig. 6c) at 17 bar. The performance is thus expected to be highly sensitive to the anchoring site. The high activity associated with the more constrained anchoring site is consistent with the observation that high temperature dehydroxylation of silica creates smaller and more active anchoring sites.[21,22,38,88,89]

Silica-anchored zirconium hydrides are reported to polymerize ethylene at near-ambient temperatures.[6,11] The calculated $\bar{P}_n$ values at the **3-3mr** ZrH site at 0.02 and 0.27 bar (Table S16 and Fig. S12b†) are consistent with these experimental observations. At higher ethylene pressures, bimolecular reactions (reactions (3c) and (3d)) as well as co-adsorbed ethylene intermediates[90] could compete with the M–C insertion and unimolecular β-H transfer reactions, introducing errors into $\bar{P}_n$.[91,92] We re-computed the TS(3a) with co-adsorbed ethylene (bim-TS(3a), Fig. S17†) and found the activation energy to be comparable to that of chain transfer to monomer (TS(3c)). The activation energy for ethylene-mediated paraffin elimination (reaction (3d), Fig. S17†) is also similar to chain transfer to the monomer (Tables S13 and S14†). Relative activation energies are consistent with prior calculations.[31,33] The activation free energies of all five termination routes at 298 and 473K are reported in Table S16† along with corresponding

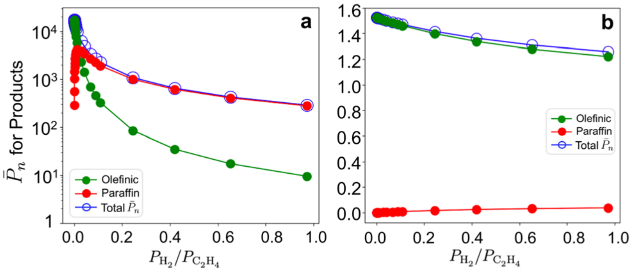

Fig. 10 Olefinic (green) and paraffinic (red) product contributions in total $\bar{P}_n$ (blue) on the **3-3mr** (≡SiO)$_3$ZrH site *vs.* $P_{H_2}/P_{C_2H_4}$ at 17 bar and (a) 298K and (b) 473K.

consequences for $\bar{P}_n$. $\bar{P}_n$ is insensitive to the incorporation of these additional routes. We conclude that the unimolecular β-H transfer is the dominant termination route and the **3-3mr** ZrH site can be tuned from a polymerization active site at room temperature to a selective oligomerization site at higher temperatures at appropriate pressures.

To evaluate the sensitivity of results to co-fed H_2, we report the $\bar{P}_n$ and olefin/paraffin contributions on the **3-3mr** site *vs.* $P_{H_2}/P_{C_2H_4}$ at 17 bar total pressure and 298 and 473 K (Fig. 10). The corresponding entropy-corrected potential energy profiles for the chain growth and two competing termination reactions are shown in Fig. S19a and b.† At 298 K (Fig. 10a), $\bar{P}_n$ decreases and the contribution of paraffinic products increases even at low hydrogen compositions (0.1 molar ratio), as with the **3-4mr** (≡SiO)$_3$ZrH site (Fig. 7). However, $\bar{P}_n$ on **3-3mr** ZrH is approximately two orders of magnitude greater than on the **3-4mr** ZrH site, even at $P_{H_2}/P_{C_2H_4} = 1$. $\bar{P}_n$ is much less sensitive to H_2 at 473 K (Fig. 10b), and the short-chain products are primarily olefinic.

We consider a third site model in which M is anchored to silica through only two oxygen linkages, constructed from a dehydroxylated (001) facet of silica (Fig. S20†). Zr(CH$_3$)$_4$ grafting energies forming (≡SiO)$_2$Zr(CH$_3$)$_2$ are intermediate between the **3-4mr** and **3-3mr** models (Fig. S21, Tables S17 and S18†) and subsequent hydrogenation is exothermic (structures in Fig. S22†). Hydrogenation to the dihydride (≡SiO)$_2$ZrH$_2$ results in a site anchored via two Zr–O–Si bonds (Fig. 11a) forming a **1-3mr** (≡SiO)$_2$ZrH$_2$ site.

The computed structures and PES for the Fig. 11b pathway are provided in Fig. S23 and S24,† respectively and the energies in Tables S19 and S20.† The availability of two Zr–H bonds offers the potential for growth of two chains. The computed barriers to insert ethylene sequentially into these two are both less than 0.1 eV. The more open coordination around Zr enables "agostic" interactions[93,94] between ethyl hydrogen atoms and Zr, evidenced in the reduced distances and angles; test calculations indicate that these interactions stabilize the intermediates by approximately 0.1 eV and cost approximately the same amount at transition states (Fig. S25†).

We computed the PES for chain growth starting from (≡SiO)$_2$ZrEt$_2$ (**2′b**, Et = ethyl) and termination to 1-butene and (≡SiO)$_2$Zr(H)Et (**2′a** in Fig. 11b). As shown in Fig. 11c, both steps have activation energies less than those on the **3-4mr** and **3-3mr** models. Fig. 9a and b show that the predicted oligomerization rates and degree of polymerization are greater on the **1-3mr** Zr-dihydride than either Zr-monohydride site. This remains true even at lower ethylene pressures and temperature where the site forms polymers (Fig. S12†).

The corresponding results for the Ti- and Hf-dihydrides are reported in the ESI† Fig. S23–S28, and Tables S19 and S20. Variations with the metal follow the same trend as found for the **3-4mr** mono-hydride sites.

4 Conclusions

Ethylene oligomerization and polymerization performance of heterogenized metal ions are known to be influenced by the

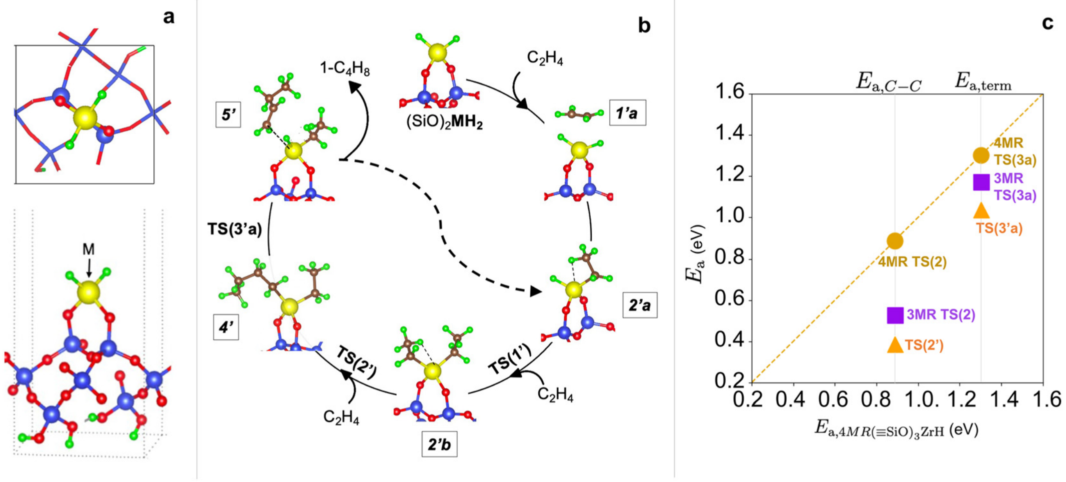

Fig. 11 (a) Top and side view of the **1-3mr** (≡SiO)$_2$MH$_2$ site. (b) Dihydride oligomerization pathways. (c) Parity plot of M–C insertion ($E_{a,C-C}$) and β-H termination ($E_{a,term}$) barriers on **3-3mr** (≡SiO)$_3$ZrH (purple squares) and **1-3mr** Zr-dihydride (orange triangles) sites against those on **3-4mr** (≡SiO)$_3$ZrH (gold circles).

metal ion identity, support morphology, and reaction conditions. Here we compare the predicted performance across the three group 4 metal ions and three different silica anchoring site models. Microkinetic models based on DFT results show that Zr has the highest intrinsic activity of the three metals (Fig. 6), as measured by the oligomerization rate, in which activity is modulated significantly by the local support environment (Fig. 9), and further that both the degree of polymerization and fraction of olefinic *vs.* paraffinic products are sensitive to co-fed H_2. Table S16 and Fig. S12† along with Fig. 9 lay out the selectivity change from polymerization to oligomerization on **3-3mr** Zr-monohydride and **1-3mr** Zr-dihydride sites going from low to high temperatures under different pressures. The results indicate that the anchored Zr ions are promising candidates for high-temperature oligomerization of ethylene, but that product selectivity will require uniformity in the anchoring site and control of temperature and hydrogen concentration.

Data availability

The data that support the findings of this study (separate folders for CONTCARs of all structures, vibrational frequency output file, transition state trajectory calculations and python scripts to create potential energy plots, rates, coverages, $\bar{P}_n$ and degree of rate control) are shared in the Zenodo data repository openly available at **https://zenodo.org/doi/10.5281/zenodo.11251372**.

Conflicts of interest

There are no conflicts to declare.

Acknowledgements

This work was financially supported by the Engineering Research Centers Program of National Science Foundation (NSF) for the project named Center for Innovative and Strategic Transformation of Alkane Resources (CISTAR) under Cooperative Agreement no. EEC-1647722. The authors would like to thank their CISTAR collaborators, in particular Jason Hicks and Galiya Magazova from University of Notre Dame for providing experimental perspective. Computing resources and technical support for this work were provided by the Notre Dame Center for Research Computing.

References

1 G. Tosin, C. C. Santini and J.-M. Basset, Polymerization of α-olefins and Hydrogenolysis of the Resulting Polyolefins with Hafnium Hydrides Supported on Silica, *Top. Catal.*, 2009, **52**, 1203–1210.

2 J. D. Pelletier and J. M. Basset, Catalysis by Design: Well-Defined Single-Site Heterogeneous Catalysts, *Acc. Chem. Res.*, 2016, **49**, 664–677.

3 L. Y. Ustynyuk, D. V. Besedin, I. E. Nifant'ev, E. A. Fushman, Y. A. Ustynyuk and V. V. Lunin, Catalytic reactions of hydrocarbons promoted by coordination unsaturated Zr and Ti compounds: A density functional theory study, *Moscow Univ. Chem. Bull.*, 2009, **64**, 343–365.

4 C. Copéret, M. Chabanas, R. Petroff Saint-Arroman and J. M. Basset, Surface organometallic chemistry: Homogeneous and heterogeneous catalysis: Bridging the gap through surface organometallic chemistry, *Angew. Chem., Int. Ed.*, 2003, **42**, 156–181.

5 V. A. Zakharov, G. A. Nesterov, S. A. Vasnetsov and K. H. Thiele, Active Centers of the Supported Organic and Hydride Transition Metal Catalysts for Ethylene Polymerization, in *Transition Metals and Organometallics as Catalysts for Olefin Polymerization*, ed. W. Kaminsky and H. Sinn, Springer, Berlin, Heidelberg, 1988, pp. 91–100.

6 V. A. Zakharov, V. K. Dudchenko, L. G. Karakchiev and Y. I. Yermakov, Formation of Zirconium hydrides in Supported OrganoZirconium Catalysts and Their Role in Ethylene Polymerization, *J. Mol. Catal.*, 1977, **2**, 421–435.

7 C. Rosier, G. P. Niccolai and J.-M. Basset, Catalytic Hydrogenolysis and Isomerization of Light Alkanes over the Silica-Supported Titanium Hydride Complex $(SiO)_3TiH$, *J. Am. Chem. Soc.*, 1997, **119**, 12408–12409.

8 J. Corker, F. Lefebvre, C. Lécuyer, V. Dufaud, F. Quignard, A. Choplin, J. Evans and J. M. Basset, Catalytic cleavage of the C-H and C-C bonds of alkanes by surface organometallic chemistry: An EXAFS and IR characterization of a Zr-H catalyst, *Science*, 1996, **271**, 966–969.

9 C. Lecuyer, F. Quignard, A. Choplin, D. Olivier and J.-M. Basset, Surface Organometallic Chemistry on Oxides: Selective Catalytic Low-Temperature Hydrogenolysis of Alkanes by a Highly Electrophilic Zirconium Hydride Complex Supported on Silica, *Angew. Chem., Int. Ed. Engl.*, 1991, **30**, 1660–1661.

10 L. d'Ornelas, S. Reyes, F. Quignard, A. Choplin and J.-M. Basset, Hafnium-Hydride Complexes Anchored to Silica. Catalysts of the Low Temperature Hydrogenolysis of Alkanes and Hydrogenation of Olefins, *Chem. Lett.*, 1993, **22**, 1931–1934.

11 F. Quignard, C. Lécuyer, A. Choplin and J.-M. Basset, From synthesis to chemical reactivity of supported d0 complexes. Part 1. An in situ infrared spectroscopic study of silica-anchored zirconium hydrides, *J. Chem. Soc., Dalton Trans.*, 1994, 1153–1158.

12 F. Quignard, C. Lécuyer, A. Choplin, D. Olivier and J.-M. Basset, Surface organometallic chemistry of zirconium: Application to the stoichiometric activation of the CH bonds of alkanes and to the low-temperature catalytic hydrogenolysis of alkanes, *J. Mol. Catal.*, 1992, **74**, 353–363.

13 V. Dufaud and J.-M. Basset, Catalytic Hydrogenolysis at Low Temperature and Pressure of Polyethylene and Polypropylene to Diesels or Lower Alkanes by a Zirconium Hydride Supported on Silica-Alumina: A Step Toward Polyolefin Degradation by the Microscopic Reverse of Ziegler-Natta Polymerization, *Angew. Chem., Int. Ed.*, 1998, **37**, 806–810.

14 C. Larabi, N. Merle, S. Norsic, M. Taoufik, A. Baudouin, C. Lucas, J. Thivolle-Cazat, A. De Mallmann and J. M. Basset, Surface organometallic chemistry of titanium on silica-

alumina and catalytic hydrogenolysis of waxes at low temperature, *Organometallics*, 2009, **28**, 5647–5655.

15 C. P. Nicholas, Applications of light olefin oligomerization to the production of fuels and chemicals, *Appl. Catal., A*, 2017, **543**, 82–97.

16 P.-A. R. Breuil, L. Magna and H. Olivier-Bourbigou, Role of Homogeneous Catalysis in Oligomerization of Olefins : Focus on Selected Examples Based on Group 4 to Group 10 Transition Metal Complexes, *Catal. Lett.*, 2015, **145**, 173–192.

17 T. Ridha, Y. Li, E. Gençer, J. J. Siirola, J. T. Miller, F. H. Ribeiro and R. Agrawal, Valorization of Shale Gas Condensate to Liquid Hydrocarbons through Catalytic Dehydrogenation and Oligomerization, *Processes*, 2018, **6**, 1–21.

18 K. C. Szeto, N. Merle, C. Rios, P. Rouge, J. L. Castelbou and M. Taoufik, Tailoring the selectivity in 2-butene conversion over supported d0 group 4, 5 and 6 metal hydrides: from dimerization to metathesis, *Catal. Sci. Technol.*, 2015, **5**, 4765–4771.

19 M. Rimoldi and A. Mezzetti, Catalysis Science & Technology Perspective Site isolated complexes of late transition metals grafted on silica: challenges and chances for synthesis and catalysis, *Catal. Sci. Technol.*, 2014, **4**, 2724–2740.

20 S. A. Holmes, F. Quignard, A. Choplin, R. Teissier and J. Kervennal, Tetraneopentyltitanium Derived Supported Catalysts Part 1. Synthesis and Catalytic Properties for the Epoxidation of Cyclohexene with Aqueous Hydrogen Peroxide, *J. Catal.*, 1998, **176**, 173–181.

21 G. Tosin, C. C. Santini, A. Baudouin, A. De Mallman, S. Fiddy, C. Dablemont and J.-M. Basset, Reactivity of Silica-Supported Hafnium Tris-neopentyl with Dihydrogen: Formation and Characterization of Silica Surface Hafnium Hydrides and Alkyl Hydride, *Organometallics*, 2007, **26**, 4118–4127.

22 C. Copéret, A. Comas-Vives, M. P. Conley, D. P. Estes, A. Fedorov, V. Mougel, H. Nagae, F. Núñez Zarur and P. A. Zhizhko, Surface Organometallic and Coordination Chemistry toward Single-Site Heterogeneous Catalysts: Strategies, Methods, Structures, and Activities, *Chem. Rev.*, 2016, **116**, 323–421.

23 F. Rataboul, A. Baudouin, C. Thieuleux, L. Veyre, C. Copéret, J. Thivolle-Cazat, J.-M. Basset, A. Lesage and L. Emsley, Molecular Understanding of the Formation of Surface Zirconium Hydrides upon Thermal Treatment under Hydrogen of $[\equiv(SiO)Zr(CH_2tBu)_3]$ by Using Advanced Solid-State NMR Techniques, *J. Am. Chem. Soc.*, 2004, **126**, 12541–12550, PMID: 15453787.

24 C. Thieuleux, E. A. Quadrelli, J. M. Basset, J. Döbler and J. Sauer, Methane activation by silica-supported Zr(IV) hydrides: The dihydride $[(\equiv SiO)_2ZrH_2]$ is much faster than the monohydride $[(\equiv SiO)_3ZrH]$, *Chem. Commun.*, 2004, 1729–1731.

25 G. Tosin, M. Delgado, A. Baudouin, C. C. Santini, F. Bayard and J. M. Basset, Surface organometallic chemistry of $Hf(CH_2tBu)_4$ on silica and silica-alumina: Reaction of the resulting grafted hafnium neopentyl with dihydrogen, *Organometallics*, 2010, **29**, 1312–1322.

26 V. A. Zakharov and Y. A. Ryndin, Surface Hydride Complexes of Group IV Transition Metals as Active Sites for Polymerization and Hydrogenation reactions, *J. Mol. Catal.*, 1989, **56**, 183–193.

27 J. J. Mortensen and M. Parrinello, A Density Functional Theory Study of a Silica-Supported Zirconium Monohydride Catalyst for Depolymerization of Polyethylene, *J. Phys. Chem. B*, 2000, **104**, 2901–2907.

28 L. Y. Ustynyuk, Y. A. Ustynyuk, D. N. Laikov and V. V. Lunin, DFT study of the mechanism of alkane hydrogenolysis by transition metal hydrides. 1. Interaction of silica-supported zirconium hydrides with methane, *Russ. Chem. Bull.*, 2001, **50**, 2050–2053.

29 C. Plascencia, L. A. Curtiss and C. Liu, Hydrogen Activation by Silica-Supported Metal Ion Catalysts: Catalytic Properties of Metals and Performance of DFT Functionals, *J. Phys. Chem. A*, 2019, **123**, 171–186.

30 A. M. Jystad, A. Biancardi and M. Caricato, Simulations of Ammonia Adsorption for the Characterization of Acid Sites in Metal-Doped Amorphous Silicates, *J. Phys. Chem. C*, 2017, **121**, 22258–22267.

31 A. Q. Kane, A. M. Esper, K. Searles, C. Ehm and A. S. Veige, Probing β-alkyl elimination and selectivity in polyolefin hydrogenolysis through DFT, *Catal. Sci. Technol.*, 2021, 6155–6162.

32 L. Y. Ustynyuk, I. A. Aleshkin, Y. V. Suleimanov, D. V. Besedin, Y. A. Ustynyuk and V. V. Lunin, The activation of C-H bonds in C1-C3 alkanes by zirconium(III,IV) and titanium(III,IV) hydrides immobilized on the surface of SiO2: a density functional theory study, *Russ. J. Phys. Chem. A*, 2007, **81**, 752–758.

33 D. V. Besedin, L. Y. Ustynyuk, Y. A. Ustynyuk and V. V. Lunin, Hydrogenolysis of alkanes and olefin polymerization on the silica-supported zirconium hydrides: A comparative DFT study, *Top. Catal.*, 2005, **32**, 47–60.

34 M. P. Kalhor, R. Wischert, C. Copéret and H. Chermette, Reactivity of silica supported zirconium hydride towards N_2O and CO_2 probe molecules: a computational point of view, *New J. Chem.*, 2014, **38**, 3717–3721.

35 F. Tielens, C. Gervais, J. F. Lambert, F. Mauri and D. Costa, Ab Initio Study of the Hydroxylated Surface of Amorphous Silica: A Representative Model, *Chem. Mater.*, 2008, **20**, 3336–3344.

36 F. Tielens, M. Gierada, J. Handzlik and M. Calatayud, Characterization of amorphous silica based catalysts using DFT computational methods, *Catal. Today*, 2020, **354**, 3–18.

37 I. S. Chuang and G. E. Maciel, A detailed model of local structure and silanol hydrogen bonding of silica gel surfaces, *J. Phys. Chem. B*, 1997, **101**, 3052–3064.

38 A. Comas-Vives, Amorphous SiO_2 surface models: energetics of the dehydroxylation process, strain, ab initio atomistic thermodynamics and IR spectroscopic signatures, *Phys. Chem. Chem. Phys.*, 2016, **18**, 7475–7482.

39 P. Ugliengo, M. Sodupe, F. Musso, I. J. Bush, R. Orlando and R. Dovesi, Realistic Models of Hydroxylated Amorphous Silica Surfaces and MCM-41 Mesoporous Material Simulated by Large-scale Periodic B3LYP Calculations, *Adv. Mater.*, 2008, **20**, 4579–4583.

40 C. S. Ewing, S. Bhavsar, G. Veser, J. J. McCarthy and J. K. Johnson, Accurate Amorphous Silica Surface Models from First-Principles Thermodynamics of Surface Dehydroxylation, *Langmuir*, 2014, **30**, 5133–5141.

41 A. Rimola, D. Costa, M. Sodupe, J.-F. Lambert and P. Ugliengo, Silica Surface Features and Their Role in the Adsorption of Biomolecules: Computational Modeling and Experiments, *Chem. Rev.*, 2013, **113**, 4216–4313.

42 P. Patel, R. H. Wells, D. M. Kaphan, M. Delferro, R. T. Skodje and C. Liu, Computational Investigation of the Role of Active Site Heterogeneity for a Supported Organovanadium(III) Hydrogenation Catalyst, *ACS Catal.*, 2021, **11**, 7257–7269.

43 S. A. Khan, S. M. Godahewa, P. N. Wimalasiri, W. H. Thompson, S. L. Scott and B. Peters, Modeling the Structural Heterogeneity of Vicinal Silanols and Its Effects on $TiCl_4$ Grafting onto Amorphous Silica, *Chem. Mater.*, 2022, **34**, 3920–3930.

44 C. S. Praveen, A. P. Borosy, C. Copéret and A. Comas-Vives, Strain in Silica-Supported Ga(III) Sites: Neither Too Much nor Too Little for Propane Dehydrogenation Catalytic Activity, *Inorg. Chem.*, 2021, **60**, 6865–6874.

45 L. Floryan, A. P. Borosy, F. Núñez-Zarur, A. Comas-Vives and C. Copéret, Strain effect and dual initiation pathway in CrIII/SiO_2 polymerization catalysts from amorphous periodic models, *J. Catal.*, 2017, **346**, 50–56.

46 U. Das, G. Zhang, B. Hu, A. S. Hock, P. C. Redfern, J. T. Miller and L. A. Curtiss, Effect of Siloxane Ring Strain and Cation Charge Density on the Formation of Coordinately Unsaturated Metal Sites on Silica: Insights from Density Functional Theory (DFT) Studies, *ACS Catal.*, 2015, **5**, 7177–7185.

47 B. Peters, S. L. Scott, A. Fong, Y. Wang and A. E. Stiegman, Reexamining the evidence for proton transfers in ethylene polymerization, *Proc. Natl. Acad. Sci. U. S. A.*, 2015, **112**, E4160–E4161.

48 A. Fong, C. Vandervelden, S. L. Scott and B. Peters, Computational Support for Phillips Catalyst Initiation via Cr–C Bond Homolysis in a Chromacyclopentane Site, *ACS Catal.*, 2018, **8**, 1728–1733.

49 C. Huang, Z. Liu, B. Liu, M. Terano and Y. Jin, Computational Insights into the Multisite Nature of the Phillips CrO_x/SiO_2 Catalyst for Ethylene Polymerization: The Perspective of Chromasiloxane Ring Size and F Modification, *ACS Catal.*, 2022, **12**, 3589–3603.

50 B. R. Goldsmith, B. Peters, J. K. Johnson, B. C. Gates and S. L. Scott, Beyond Ordered Materials: Understanding Catalytic Sites on Amorphous Solids, *ACS Catal.*, 2017, **7**, 7543–7557.

51 P. Cossee, Ziegler-Natta Catalysis I. Mechanism of Polymerization of α-Olefins with Ziegler-Natta Catalysts, *J. Catal.*, 1964, **3**, 80–88.

52 D. R. Burfield, Ziegler-Natta polymerization: The nature of the propagation step, *Polymer*, 1984, **25**, 1645–1654.

53 V. I. Avdeev, I. I. Zakharov, V. A. Zakharov, G. D. Bukatov and Y. I. Ermakov, Quantum-chemical study of the mechanism of the growth reaction in the catalytic polymerization of alkenes, *J. Struct. Chem.*, 1977, **18**, 420–436.

54 T. K. Woo, L. Fan and T. Ziegler, A Density Functional Study of Chain Growing and Chain Terminating Steps in Olefin Polymerization by Metallocene and Constrained Geometry Catalysts, *Organometallics*, 1994, **13**, 2252–2261.

55 M. E. O'Reilly, S. Dutta and A. S. Veige, β-Alkyl Elimination: Fundamental Principles and Some Applications, *Chem. Rev.*, 2016, **116**, 8105–8145.

56 L. Cavallo, G. Guerra and P. Corradini, Mechanisms of Propagation and Termination Reactions in Classical Heterogeneous Ziegler-Natta Catalytic Systems: A Nonlocal Density Functional Study, *J. Am. Chem. Soc.*, 1998, **120**, 2428–2436.

57 W. Kaminsky and H. Lüker, Influence of hydrogen on the polymerization of ethylene with the homogeneous ziegler system bis(cyclopentadienyl)zirconiumdichloride/aluminoxane, *Makromol. Chem., Rapid Commun.*, 1984, **5**, 225–228.

58 A. S. Hoffman, B. A. Fries and P. C. Condit, The role of hydrogen in ziegler-natta polymerizations, *J. Polym. Sci., Part C: Polym. Symp.*, 1963, **4**, 109–126.

59 Y. V. Kissin, L. A. Rishina and E. I. Vizen, Hydrogen effects in propylene polymerization reactions with titanium-based Ziegler–Natta catalysts. II. Mechanism of the chaintransfer reaction, *J. Polym. Sci., Part A: Polym. Chem.*, 2002, **40**, 1899–1911.

60 G. Kresse and J. Hafner, Ab initio molecular dynamics for liquid metals, *Phys. Rev. B*, 1993, **47**, 558–561.

61 G. Kresse and J. Hafner, Ab initio molecular-dynamics simulation of the liquid-metal–amorphous-semiconductor transition in germanium, *Phys. Rev. B*, 1994, **49**, 14251–14269.

62 G. Kresse and J. Furthmüller, Efficiency of ab-initio total energy calculations for metals and semiconductors using a plane-wave basis set, *Comput. Mater. Sci.*, 1996, **6**, 15–50.

63 G. Kresse and J. Furthmüller, Efficient iterative schemes for ab initio total-energy calculations using a plane-wave basis set, *Phys. Rev. B*, 1996, **54**, 11169–11186.

64 P. E. Blöchl, Projector augmented-wave method, *Phys. Rev. B*, 1994, **50**, 17953–17979.

65 J. P. Perdew, K. Burke and M. Ernzerhof, Generalized gradient approximation made simple, *Phys. Rev. Lett.*, 1996, **77**, 3865–3868.

66 J. P. Perdew, K. Burke and M. Ernzerhof, Generalized Gradient Approximation Made Simple, *Phys. Rev. Lett.*, 1996, **77**, 3865 (*Phys. Rev. Lett.*, 1997, **78**, 1396–1396).

67 G. Henkelman and H. Jónsson, Improved tangent estimate in the nudged elastic band method for finding minimum energy paths and saddle points, *J. Chem. Phys.*, 2000, **113**, 9978–9985.

68 G. Henkelman, B. P. Uberuaga and H. Jónsson, Climbing image nudged elastic band method for finding saddle points and minimum energy paths, *J. Chem. Phys.*, 2000, **113**, 9901–9904.

69 G. Henkelman and H. Jönsson, A dimer method for finding saddle points on high dimensional potential surfaces using only first derivatives, *J. Chem. Phys.*, 1999, **111**, 7010–7022.

70 A. H. Larsen, *et al.*, The atomic simulation environment—a Python library for working with atoms, *J. Phys.: Condens. Matter*, 2017, **29**, 273002.

71 K. Momma and F. Izumi, VESTA: a three-dimensional visualization system for electronic and structural analysis, *J. Appl. Crystallogr.*, 2008, **41**, 653–658.

72 R. W. G. Wyckoff, *Crystal Structures*, John Wiley & Sons, 2nd edn, 1963, ch. 4, vol. 1, pp. 239–444.

73 L. He, F. Liu, G. Hautier, M. J. T. Oliveira, M. A. L. Marques, F. D. Vila, J. J. Rehr, G.-M. Rignanese and A. Zhou, Accuracy of generalized gradient approximation functionals for density-functional perturbation theory calculations, *Phys. Rev. B*, 2014, **89**, 064305.

74 X. Rozanska, F. Delbecq and P. Sautet, Reconstruction and stability of β-cristobalite 001, 101, and 111 surfaces during dehydroxylation, *Phys. Chem. Chem. Phys.*, 2010, **12**, 14930–14940.

75 A. Meurer, *et al.*, SymPy: symbolic computing in Python, *PeerJ Comput. Sci.*, 2017, **3**, e103.

76 G. Van Rossum and F. L. Drake, *Python 3 Reference Manual*, CreateSpace, Scotts Valley, CA, 2009.

77 K. Toch, J. Thybaut and G. Marin, Ethene oligomerization on Ni-SiO_2-Al_2O_3: Experimental investigation and Single-Event MicroKinetic modeling, *Appl. Catal., A*, 2015, **489**, 292–304.

78 C. J. Cramer, *Essentials of Computational Chemistry: Theories and Models*, John Wiley, 2nd edn, 2004, ch. 2, pp. 22–44.

79 C. T. Campbell and J. R. Sellers, The entropies of adsorbed molecules, *J. Am. Chem. Soc.*, 2012, **134**, 18109–18115.

80 P. J. Davidson, M. F. Lappert and R. Pearce, Metal σ-Hydrocarbyls, MRn Stoichiometry, Structures, Stabilities, and Thermal Decomposition Pathways, *Chem. Rev.*, 1976, **76**, 219–242.

81 N. Greenwood and A. Earnshaw, *Chemistry of Elements*, Pergamon Press, 2nd edn, 1989, ch. 4, pp. 220–329.

82 G. Tosin, C. C. Santini, M. Taoufik, A. De Mallmann and J. M. Basset, Reactivity of tetraneopentylhafnium, $Hf(CH_2tBu)_4$, with silica surfaces, *Organometallics*, 2006, **25**, 3324–3335.

83 R. Robinson, D. S. McGuinness and B. F. Yates, The mechanism of ethylene dimerization with the $Ti(OR)_4/AlR_3$ catalytic system: DFT studies comparing metallacycle and Cossee proposals, *ACS Catal.*, 2013, **3**, 3006–3015.

84 L. C. Grabow, in *Computational Catalysis*, ed. A. Asthagiri and M. J. Janik, The Royal Society of Chemistry, 2013, pp. 1–58.

85 A. Fong, Y. Yuan, S. L. Ivry, S. L. Scott and B. Peters, Computational kinetic discrimination of ethylene polymerization mechanisms for the Phillips (Cr/SiO_2) catalyst, *ACS Catal.*, 2015, **5**, 3360–3374.

86 G. J. Britovsek, R. Malinowski, D. S. McGuinness, J. D. Nobbs, A. K. Tomov, A. W. Wadsley and C. T. Young, Ethylene Oligomerization beyond Schulz-Flory Distributions, *ACS Catal.*, 2015, **5**, 6922–6925.

87 D. P. Lo and W. H. Ray, Kinetic modeling and prediction of polymer properties for ethylene polymerization over nickel diimine catalysts, *Ind. Eng. Chem. Res.*, 2005, **44**, 5932–5949.

88 L. Zhuravlev, The surface chemistry of amorphous silica. Zhuravlev model, *Colloids Surf., A*, 2000, **173**, 1–38.

89 J. H. Z. dos Santos, C. Krug, M. B. da Rosa, F. C. Stedile, J. Dupont and M. de Camargo Forte, The effect of silica dehydroxylation temperature on the activity of SiO_2-supported zirconocene catalysts, *J. Mol. Catal. A: Chem.*, 1999, **139**, 199–207.

90 L. Cavallo and G. Guerra, A Density Functional and Molecular Mechanics Study Of β-Hydrogen Transfer in Homogeneous Ziegler-Natta Catalysis, *Macromolecules*, 1996, **29**, 2729–2737.

91 J. N. Harvey, F. Himo, F. Maseras and L. Perrin, Scope and Challenge of Computational Methods for Studying Mechanism and Reactivity in Homogeneous Catalysis, *ACS Catal.*, 2019, **9**, 6803–6813.

92 G. Talarico and P. H. M. Budzelaar, Variability of Chain Transfer to Monomer Step in Olefin Polymerization, *Organometallics*, 2008, **27**, 4098–4107.

93 J. C. W. Lohrenz, T. K. Woo and T. Ziegler, A Density Functional Study on the Origin of the Propagation Barrier in the Homogeneous Ethylene Polymerization with Kaminsky-Type Catalysts, *J. Am. Chem. Soc.*, 1995, **117**, 12793–12800.

94 M. Brookhart, M. L. H. Green and G. Parkin, Agostic interactions in transition metal compounds, *Proc. Natl. Acad. Sci. U. S. A.*, 2007, **104**, 6908–6914.